IOP Publishing Phys. Med. Biol. 65 (2020) 235022 https://doi.org/10.1088/1361-6560/abb31d

Physics in Medicine & Biology

IPEM Institute of Physics and Engineering in Medicine

PAPER

RECEIVED
1 June 2020

REVISED
18 August 2020

ACCEPTED FOR PUBLICATION
27 August 2020

PUBLISHED
25 November 2020

Motion correction for PET data using subspace-based real-time MR imaging in simultaneous PET/MR

Thibault Marin[1,2,4], **Yanis Djebra**[1,2,3,4], **Paul K Han**[1,2], **Yanis Chemli**[1,2,3], **Isabelle Bloch**[3], **Georges El Fakhri**[1,2], **Jinsong Ouyang**[1,2], **Yoann Petibon**[1,2] and **Chao Ma**[1,2,5]

[1] Gordon Center for Medical Imaging, Department of Radiology, Massachusetts General Hospital, Boston MA, 02114, United States of America
[2] Harvard Medical School, Boston MA, 02115, United States of America
[3] LTCI, Télécom Paris, Institut Polytechnique de Paris, France
[4] Equal contribution
[5] Corresponding author

E-mail: thibault.marin.us@ieee.org

Keywords: PET motion correction, subspace modeling, low-rank reconstruction, PET/MR

Supplementary material for this article is available online

Abstract

Image quality of positron emission tomography (PET) reconstructions is degraded by subject motion occurring during the acquisition. Magnetic resonance (MR)-based motion correction approaches have been studied for PET/MR scanners and have been successful at capturing regular motion patterns, when used in conjunction with surrogate signals (e.g. navigators) to detect motion. However, handling irregular respiratory motion and bulk motion remains challenging. In this work, we propose an MR-based motion correction method relying on subspace-based real-time MR imaging to estimate motion fields used to correct PET reconstructions. We take advantage of the low-rank characteristics of dynamic MR images to reconstruct high-resolution MR images at high frame rates from highly undersampled k-space data. Reconstructed dynamic MR images are used to determine motion phases for PET reconstruction and estimate phase-to-phase nonrigid motion fields able to capture complex motion patterns such as irregular respiratory and bulk motion. MR-derived binning and motion fields are used for PET reconstruction to generate motion-corrected PET images. The proposed method was evaluated on *in vivo* data with irregular motion patterns. MR reconstructions accurately captured motion, outperforming state-of-the-art dynamic MR reconstruction techniques. Evaluation of PET reconstructions demonstrated the benefits of the proposed method in terms of motion artifacts reduction, improving the contrast-to-noise ratio by up to a factor 3 and achieveing a target-to-background ratio up to 90% superior compared to standard/uncorrected methods. The proposed method can improve the image quality of motion-corrected PET reconstructions in clinical applications.

1. Introduction

Motion, including physiological motion (*i.e.* cardiac and respiratory motions) and involuntary bulk motion, is a major source of image quality degradation in positron emission tomography (PET), which can result in spatial blurring artifacts and mismatch between emission and attenuation maps, altering quantification of tracer concentration and deteriorating the diagnostic value of PET images (Liu *et al* 2009, Ouyang *et al* 2013, Rubeaux *et al* 2017). The conventional way to handle motion in PET is the gating method, which bins PET list-mode data to different cardiac and/or respiratory motion phases followed by reconstructions of images of each phase. However, gating results in increased noise levels due to the reduced number of events in each motion phase. To address the limitations of the gating method, many PET motion correction methods have been developed, which consist of two consecutive steps: motion field estimation and motion correction by

© 2020 Institute of Physics and Engineering in Medicine

either applying the estimated motion field to the gated images or modeling it within motion-compensated PET image reconstruction (Rahmim *et al* 2013).

PET motion correction methods can be divided into two major subcategories, depending on how the motion field is estimated: PET-based methods and magnetic resonance (MR)-based methods. In the PET-based motion correction methods, the measured emission data are first assigned to specific motion phases based on surrogate signals (Jin *et al* 2013), *e.g.* electrocardiogram (EKG), respiratory bellow, optical tracking, etc. (Fulton *et al* 2002, Montgomery *et al* 2006, Yu *et al* 2016), or the PET-data themselves (Kesner *et al* 2009, Sun *et al* 2019, Lu *et al* 2019), *e.g.* center of mass, time-of-flight information, frame-by-frame images, etc. Motion fields are then estimated by registering the reconstructed image of each phase to a reference phase (Dawood *et al* 2008). However, the accuracy of the motion fields estimated by the PET-based methods is limited by low signal-to-noise ratio (SNR), especially in the case of dual gating, and the overall lack of anatomical structural information of PET images (Ouyang *et al* 2013, Petibon *et al* 2019).

The increasing availability of hybrid PET/MR systems provides a unique opportunity for mitigating effects of motion in PET using MR-based motion correction. Because of its excellent soft-tissue contrast, high spatial resolution, and high SNR, MR provides more accurate estimation of motion fields than the PET-based methods. MR-based PET motion correction methods have been successfully applied to compensate respiratory and cardiac motion in various applications involving both static and dynamic PET imaging (Petibon *et al* 2013, Huang *et al* 2014, Petibon *et al* 2019, Catana 2015, Gillman *et al* 2017, Küstner *et al* 2017). One major limitation of the MR-based motion correction methods is that the conventional noniterative MR imaging methods are unable to resolve cardiac or respiratory motion in real time due to the slow imaging speed. Binning-based MR imaging methods (Grimm *et al* 2015, Rank *et al* 2016, Feng *et al* 2016, Munoz *et al* 2018, Robson *et al* 2018) are often used to address this issue, where MR k-space data are grouped into different motion phases based on surrogate signals (e.g. EKG), navigator signals, or k-space data alone, and images of each motion phase are then reconstructed for the estimation of motion fields. However, the binning-based MR imaging methods suffer from three noticeable limitations. First, they assume pseudo periodic motion, which does not hold well in the case of arrhythmia and irregular respiratory motion. Second, they rely on either surrogate signals or navigator signals acquired along a single direction to assign k-space data to specific motion phases, which cannot reliably capture involuntary bulk motion. Third, their performance is limited by the inherent trade-off between the number of motion phases (and thus the accuracy of motion field measurement) and data acquisition time.

In this work, we propose a real-time MR imaging method for PET motion corrections in PET/MR. High resolution real-time MR imaging is achieved by a subspace-based imaging method, which takes advantage of a unique property of high-dimensional dynamic MR signals known as partial separability (PS) (Liang 2007). The PS-model takes advantage of the spatial-temporal correlations of dynamic MR images, significantly reduces the number of unknowns of the underlying spatiotemporal signal, and makes it possible to recover high resolution, high frame-rate dynamic MR images from highly undersampled k-space data (Zhao *et al* 2012, Christodoulou *et al* 2014). For PET motion correction, the reconstructed real-time MR images are used to determine motion phases and estimate motion fields. PET list-mode data are binned into sinograms accordingly and ordered-subset expectation-maximization (OSEM) reconstruction (Hudson and Larkin 1994) is performed integrating the estimated displacement in the system matrix for motion correction. We demonstrate the performance of the proposed method by carrying out *in vivo* ^{18}F-FDG PET/MR imaging experiments using a 3 T simultaneous PET/MR scanner.

2. Methods

2.1. PET/MR imaging experiment

An ^{18}F-FDG PET/MR scan was performed on one healthy subject under a study protocol approved by our local IRB. PET and MR data were simultaneously acquired 30 minutes after ^{18}F-FDG injection (around 10 mCi) using a 3 T PET/MR scanner (Siemens Biograph mMR, Siemens Healthcare, Erlangen, Germany).

Two 5-minute MR acquisitions were performed using a spoiled gradient-recalled echo (GRE) sequence with stack-of-stars radial sampling trajectories in the coronal plane. The imaging parameters are as follows: image size $= 384 \times 384 \times 32$, resolution $= 1.9 \times 1.9 \times 5$ mm^3, TR/TE $= 3/1.6$ ms, and flip angle $= 7$ degrees. The (k,t)-space data were acquired using a random sampling pattern shown in figure 1. A total of 35 k-space spokes were sampled in each frame, resulting in a frame rate of 9.5 volumes per second. For each frame, the first 3 spokes were respectively acquired along the k_x, k_y and k_z direction across the center of the k-space to estimate the temporal basis of the partially separable (PS) model detailed next. The remaining 32 spokes were along a random angle in the k_x-k_y plane for every k_z. During the first 5-minute acquisition, the subject was instructed to move once to assess the effect of both respiratory and bulk motion. During the second 5-minute acquisition, the subject was instructed to simulate an irregular respiratory pattern including both

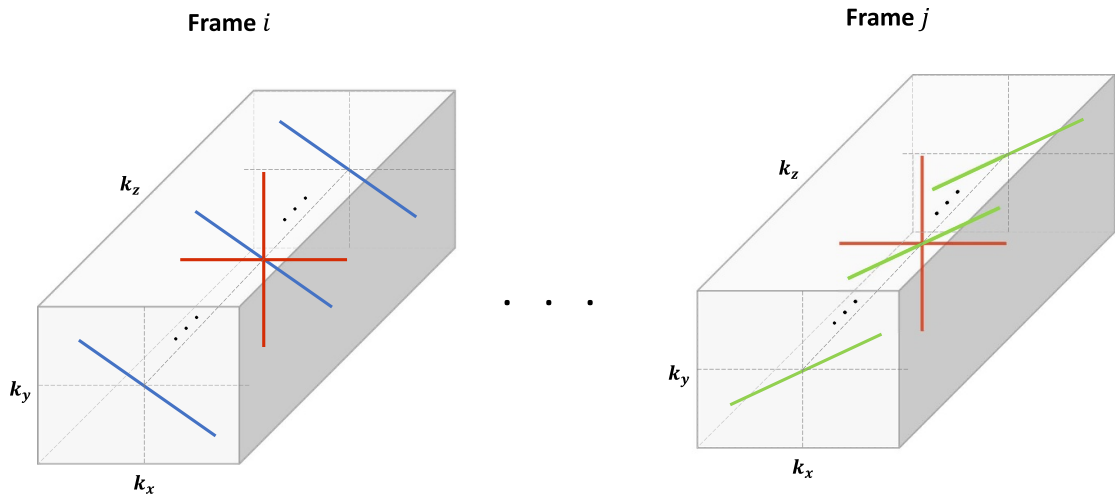

Figure 1. MR Sampling scheme used for the proposed method. 35 lines per frame are acquired: 1 line along k_z and 34 lines in the k_x-k_y plane. For a better visibility, only the k_x-k_y in-plane acquired lines are shown in the figure. Two training lines along k_x and k_y at $k_z = 0$ are consistently acquired through the whole acquisition to estimate the temporal basis V_t (red lines). A random angle is chosen every frame and is consistently acquired every k_z for imaging.

deep and shallow breaths. The vendor-provided two-point Dixon sequence was performed with breath-holding to obtain attenuation coefficients.

2.2. Subspace-based image reconstruction

Denote the dynamic image series as $\rho(\boldsymbol{r}, t)$ and its matrix representation $\boldsymbol{C} \in \mathbb{C}^{N\times M}$ such that:

$$\boldsymbol{C} = \begin{bmatrix} \rho(\boldsymbol{r}_1, t_1) & \dots & \rho(\boldsymbol{r}_1, t_M) \\ \vdots & \ddots & \vdots \\ \rho(\boldsymbol{r}_N, t_1) & \dots & \rho(\boldsymbol{r}_N, t_M) \end{bmatrix}. \tag{1}$$

We express $\rho(\boldsymbol{r}, t)$ as a PS model (Liang 2007):

$$\rho(\boldsymbol{r}, t) = \sum_{l=1}^{L} u_l(\boldsymbol{r}) v_l(t), \tag{2}$$

or, equivalently C as:

$$\boldsymbol{C} = U_s V_t, \tag{3}$$

where $V_t \in \mathbb{C}^{L\times M}$ concentrates in rows the temporal basis function v_l of the PS model up to order L and $U_s \in \mathbb{C}^{N\times L}$ concentrates in columns the corresponding spatial coefficients u_l.

We estimate the temporal basis functions using the training data acquired at every frame. Assuming p training lines, we form the so-called Casorati matrix $\boldsymbol{C}_t \in \mathbb{C}^{pN_f\times M}$ by stacking the signal of the p training lines at each frame, where N_f is the number of samples acquired in each k-space line. The temporal basis functions $\{v_l\}_{l=1}^{L}$ can then be estimated by calculating the first L right eigenvectors of $\boldsymbol{C}_t$ using singular value decomposition (SVD).

Once V_t is obtained (denoted by $\hat{V}_t$), the image reconstruction problem is reduced to the determination of the spatial coefficients matrix U_s. We solve this problem by fitting the PS model to the undersampled (k,t)-space data with additional sparsity constraints (Zhao *et al* 2012):

$$\hat{U}_s = \arg\min_{U_s} \left\| d - \Omega\left(F_s U_s \hat{V}_t\right) \right\|_2^2 + \lambda_1 \left\| T(U_s \hat{V}_t) \right\|_1 + \lambda_2 \left\| U_s \right\|_F, \tag{4}$$

where d is the measured k-space data, F_s is the Fourier transform operator in the spatial domain, *i.e.* Non-Uniform FFT (NUFFT) operator (Fessler and Sutton 2003) for the stack-of-stars trajectory, Ω is the sparse sampling operator in the (k,t)-space, T is the finite difference operator along both the spatial and temporal directions, $\|.\|_F$ is the Frobenius norm and the scalar variables λ_1 and λ_2 are regularization parameters. The first term in equation (4) is a data fidelity term, the second term promotes sparsity in the reconstructed image and the third term favors minimal norm solutions for U_s.

We solve the optimization problem in equation (4) using the alternating direction methods of multipliers (ADMM) algorithm (Boyd *et al* 2011), which leads to solving the following three sub-optimization problems in an alternative fashion:

$$z^{(k+1)} = \mathcal{S}_{\frac{\lambda_1}{\mu}}\left(T\left(U_s^{(k)}\hat{V}_t\right) + \eta^{(k)}\right), \tag{5}$$

$$U_s^{(k+1)} = \arg\min_{U_s} \frac{1}{2}\left\|d - \Omega\left(F_s U_s \hat{V}_t\right)\right\|_2^2 + \frac{\mu}{2}\left\|T\left(U_s\hat{V}_t\right) - z^{(k+1)} + \eta^{(k)}\right\|_F^2 + \lambda_2\left\|U_s\right\|_F, \tag{6}$$

$$\eta^{(k+1)} = \eta^{(k)} + \left(T\left(U_s^{(k+1)}\hat{V}_t\right) - z^{(k+1)}\right),$$

where z is the split variable, η is the dual variable, and μ is a scalar relaxation parameter. The z update in equation (5) is a soft thresholding operation and the U_s update equation (6) is a convex-optimization problem, which is solved using the conjugate gradient algorithm.

For comparison, we reconstructed MR images using the same data by a binning-based method, known as XD-GRASP (Feng *et al* 2016). The respiratory motion signal used for binning was processed the same way Feng *et al* (2016) did: the Fourier transform of the data at the center of the k-space at each frame was sorted into a 2D matrix, with data from each coil concatenated along the first dimension. A Principal Component Analysis (PCA) was then applied on this matrix and the component with the highest peak in the respiratory frequency range (0.1, 0.5 Hz) was selected as the binning signal. The k-space data were then regrouped into balanced bins, *i.e.* each bin containing the same number of spokes. The actual number of bins is experiment dependent and will be described later in the Results section. The XD-GRASP reconstruction was performed the same way as in Feng *et al* (2016).

2.3. Motion estimation

The reconstructed real-time MR images were first binned into a small number of phases corresponding to different body positions (respiratory and bulk motion phases). Binning was performed in three steps. The first step consists in visually determining the bulk motion phases from the MR images and discarding time frames corresponding to the transition between bulk motion phases. In the second step, a bin is assigned to each (real-time) frame by tracking the tip of the right lobe of the liver over time while ensuring balanced bins (*i.e.*, all bins should contain a similar number of frames). Finally, a combined MR image is formed for each bin by averaging all real-time images in a bin. Volumetric image registration was then performed between all bins and a reference bin using the multiscale B-spline registration algorithm described by Chun and Fessler (2009).

2.4. PET reconstruction

The acquired list-mode PET events were first rearranged into B sinograms $\boldsymbol{y} = (\boldsymbol{y}_1, \ldots, \boldsymbol{y}_B)$ following the binning determined from MR images and discarding PET list-mode events occurring during bulk motion transitions.

PET reconstruction was performed using the OSEM algorithm (Hudson and Larkin 1994) integrating the estimated motion fields in the forward model (Liu *et al* 2011, Petibon *et al* 2016). Let $\boldsymbol{x}$ denote the PET image to reconstruct arranged in vector form. The system matrix, denoted by $\boldsymbol{F}$, is decomposed as $\boldsymbol{F} = \boldsymbol{SAGM}$, where:

- $\boldsymbol{M} = [\boldsymbol{M}_1, \ldots, \boldsymbol{M}_B]^\top$ is a stack of deformation operators estimated using the procedure described in Section 2.3,
- $\boldsymbol{G} = \mathrm{diag}(\overline{\boldsymbol{G}}, \ldots, \overline{\boldsymbol{G}})$ is a block-diagonal geometrical projection matrix constructed by repeating the static projection matrix $\overline{\boldsymbol{G}}$ implemented using Siddon's algorithm (Siddon 1985),
- $\boldsymbol{A} = \mathrm{diag}(\boldsymbol{A}_1, \ldots, \boldsymbol{A}_B)$ is a diagonal matrix with time-varying attenuation coefficients,
- $\boldsymbol{S} = \mathrm{diag}(\overline{\boldsymbol{S}}, \ldots, \overline{\boldsymbol{S}})$ is a diagonal matrix with detector sensitivity coefficients $\overline{\boldsymbol{S}}$ repeated for all bins.

With these notations, the motion-corrected OSEM update for a given subset l is given by:

$$\boldsymbol{x}^{(n+1)} = \frac{\boldsymbol{x}^{(n)}}{\boldsymbol{F}_l^\top \mathbb{1}} \boldsymbol{F}_l^\top \frac{\boldsymbol{y}_l}{\boldsymbol{F}_l \boldsymbol{x}^{(n)} + \boldsymbol{s}_l}, \tag{8}$$

where $\boldsymbol{F}_l$ is the system matrix for the lth subset and $\boldsymbol{s}_l$ is the combined additive correction sinogram for subset l including randoms and scatter. Correction sinograms were constructed as follows. Random coincidences

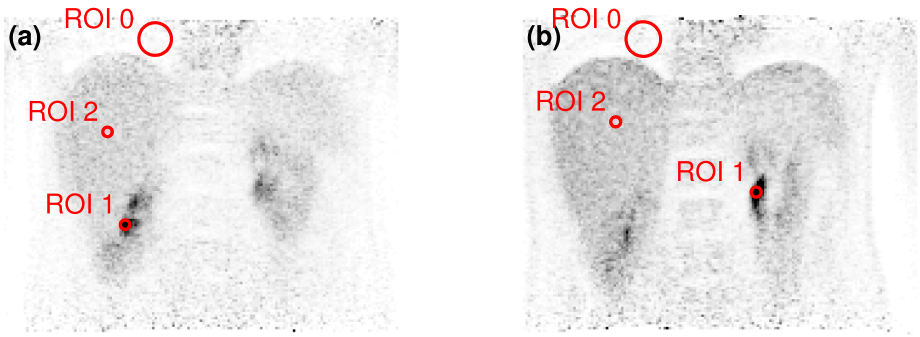

Figure 2. Regions of interest used for quantitative analysis: (a) bulk motion experiment, (b) irregular respiratory motion experiment. ROI 0 in the lung, ROI 1 in the kidney, ROI 2 in the liver. For each experiment a small region in the kidney with the highest activity was selected to assess the effects of different PET reconstruction methods on contrast-to-noise ratio.

were estimated using the delayed window method. Scatter was estimated using the single scatter simulation algorithm (Werling *et al* 2002) from an initial reconstruction performed without motion correction. Scatter was estimated separately for each bulk motion phase. Attenuation coefficients were obtained from a vendor-provided Dixon sequence during breath-holding. The attenuation map was deformed to each bin and forward projected to calculate sinogram-domain attenuation coefficients.

The OSEM used 12 subsets and 5 iterations. This motion-corrected reconstruction is denoted by MC in the rest of the paper. For comparison, two other reconstruction methods were considered: a traditional OSEM without motion correction (NMC) and a gated reconstruction where only list-mode events occurring in a given motion phase are reconstructed without motion correction (Gated). Note that no time-of-flight information was available and that the scanner's point spread function was not included in the imaging model. Both reference methods used 4 iterations to account for the difference in convergence speed, aiming to match the noise level in MC and NMC reconstructions. The noise level was not matched for the Gated method in order to keep gated reconstructions sharp and better compare with motion correction methods (in practice gated reconstruction would typically use fewer subsets and/or iterations).

2.5. Quantitative analysis

In order to compare PET reconstructions, two evaluation measures were used: the contrast-to-noise ratio (CNR) and target-to-background ratio (TBR). The contrast-to-noise ratio is defined as:

$$\mathrm{CNR}(x,\mathcal{R}) = \frac{\bar{x}_{\mathcal{R}} - \bar{x}_{\mathcal{R}_0}}{\sigma_0}, \tag{9}$$

where σ_0 is the standard deviation in the background region $\mathcal{R}_0$ and $\bar{x}_{\mathcal{R}}$ is the average activity of image x in region $\mathcal{R}$. The background region $\mathcal{R}_0$ was a spherical region with a diameter of 14 mm, which was placed in a low activity region (lung) and defined large enough to estimate the noise level. With the same notations, the target-to-background ratio is given by:

$$\mathrm{TBR}(x,\mathcal{R}) = \frac{\bar{x}_{\mathcal{R}}}{\bar{x}_{\mathcal{R}_2}}, \tag{10}$$

where $\mathcal{R}_2$ is a small spherical region with diameter 4 mm located in the liver. Both measures were evaluated in a small spherical region with diameter 4 mm located in the kidney ($\mathcal{R}_1$ shown in figure 2). The region was selected in the kidney with the highest activity and its size was defined to cover the high activity region. Note that all regions of interest were located at the same position for all reconstruction methods. In the absence of ground truth, the contrast-to-noise and target-to-background ratios were used as indicators of image quality.

3. Results

3.1. Correction of bulk motion

In this experiment the subject was instructed to move after around 2.5 minutes in the 5-minute acquisition. Images reconstructed by XD-GRASP and the proposed method at the end-inhalation and end-exhalation phases are shown in figure 3. The k-space data were grouped into six balanced bins as in Feng *et al* (2016) in the XD-GRASP reconstruction. The images obtained by XD-GRASP method show noticeable blurring artifacts largely because the bulk motion was not detected from the navigator signal. More specifically, figure 4(a) shows the navigator signal obtained from the training line along the k_z direction in each frame as in

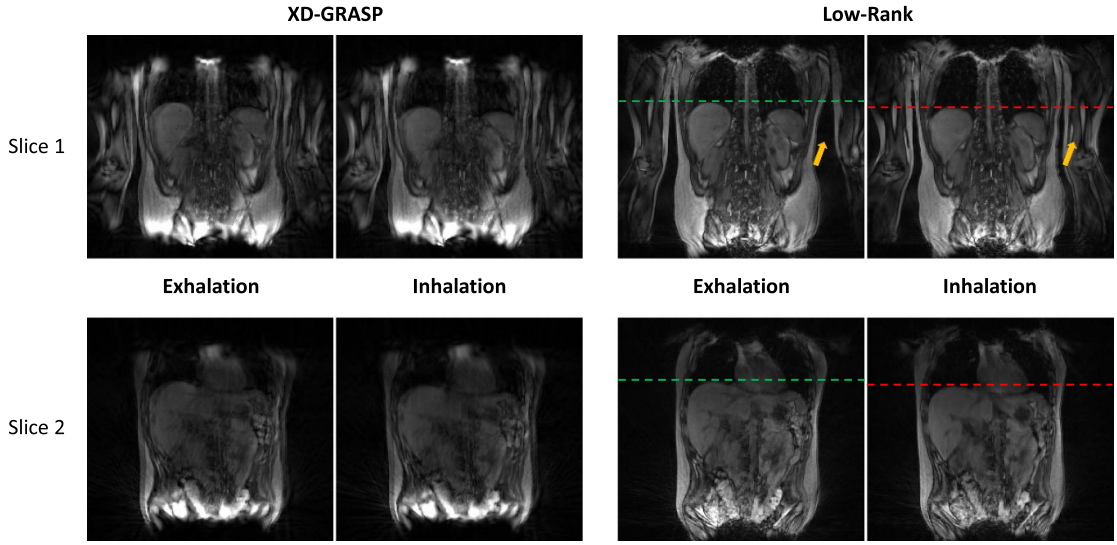

Figure 3. Representative MR images obtained with the XD-GRASP and the proposed method. The red dashed-line indicates the top of the liver position for end-inhalation and the green dashed-line indicates the top of the liver position for end-exhalation. Note that, besides respiratory motion, bulk motion indicated by the yellow arrows is clearly seen in the proposed low-rank based image reconstruction. The images obtained by XD-GRASP show blurring artifacts largely because the bulk motion was not detected from the navigator signal (see figure 4 for more details).

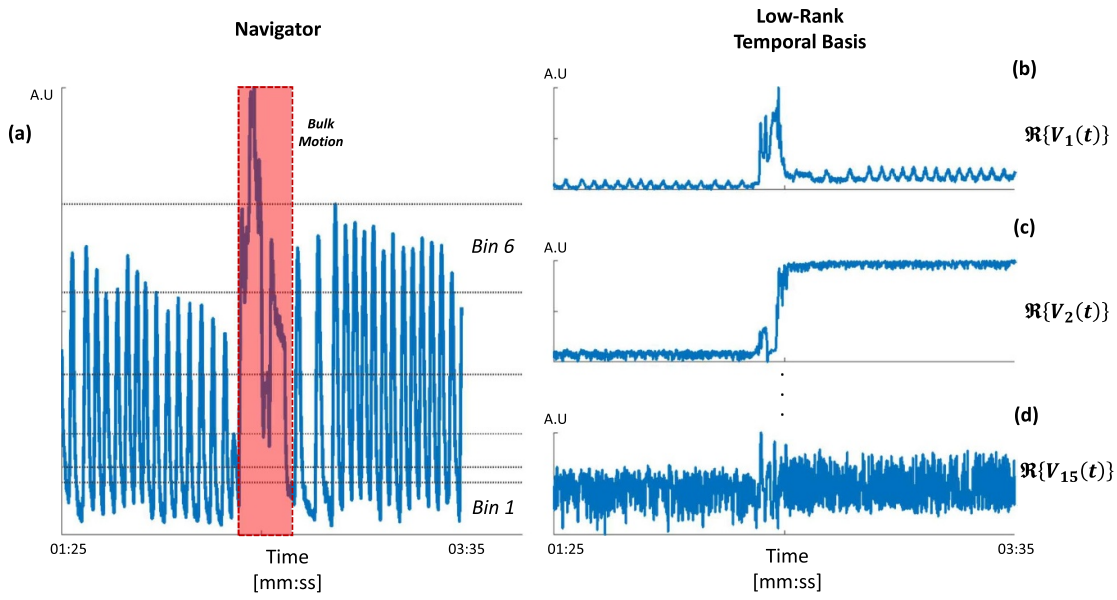

Figure 4. (a) Plot of the processed navigator along time, which was used to bin the k-space data in XD-GRASP. (b) to (d) Real part of the temporal basis V_t for the component 1, 2, and 15 of the PS model, respectively.

Feng *et al* (2016). Since the bulk motion of the subject was along the x direction (left to right), the navigator signal only recorded abnormal changes during the bulk motion, *i.e.* the red region in figure 4(a), but did not contain sufficient information to indicate what type of motion occurred. Therefore, six motion bins were chosen in XD-GRASP while the k-space data acquired in the red region of figure 4(a) were discarded, resulting in blurring artifacts.

The images obtained by the proposed method shown in figure 3 successfully capture both respiratory motion (as indicated by the red and green dashed lines) and bulk motion (as indicated by the yellow arrows). Figure 4(b)–(d) show the temporal basis functions of the PS model estimated from the three training lines, where, intuitively, the first component (figure 4(b)) shows respiratory patterns and the second component (figure 4(c)) indicates bulk motion. To further demonstrate the real-time capabilities of the proposed method, figure 5 shows images at multiple time frames along with a 1D profile through the liver along time. The images from before and after bulk motion demonstrate the ability to capture both respiratory and bulk motion. The yellow overlay emphasizes the body displacement between Stage 1 and Stage 2. The profile plot

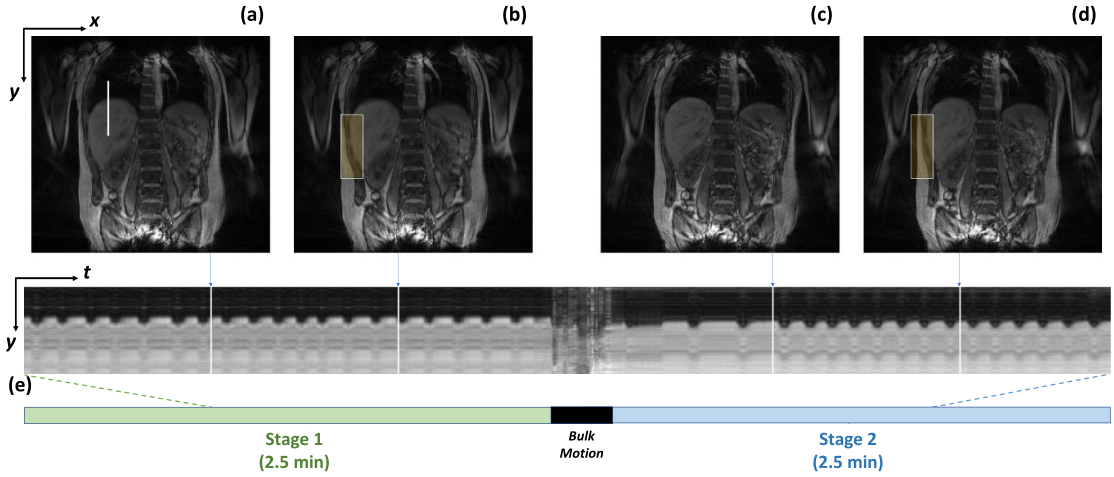

Figure 5. Dynamic MR images reconstructed by the proposed method. The real-time profile (e) is plotted for a part of the experiment where the bulk motion happens, and two representative images (a) & (b) and (c) & (d) are shown for each body position. The white line in (a) shows where the time profile was taken. A yellow box at the edge of the patient has been drawn for the first body position (b) and the same box was also drawn for the second body position (d) at the same coordinates (regarding the image). One can clearly see that the body of the subject moved to the right of the image during the bulk motion, and that the proposed method managed to catch that motion.

shows the respiratory motion, captured for both bulk motion phases. The transition portion between the two bulk motion phases corresponds to the frames that were discarded in the PET reconstruction. Videos showing the reconstructed MR images are available in the Supplementary Material M1 (stacks.iop.org/PMB/65/235022/mmedia).

To account for the two body positions and for respiratory motion in PET reconstruction, real-time MR images obtained by the proposed method were grouped into 12 bins (six bins for each body position) for motion field estimation. Frames in the transition between the two bulk motion phases were excluded (a total of 15 seconds were discarded). Motion was estimated between all bins and the bin corresponding to the end-exhalation, which was used as reference bin. Estimated motion fields are shown in figure 6. The top left image shows motion caused by respiration, mostly visible as a vertical displacement near the liver (shown with more details in the inset image). The left column images show the bulk motion, which is mostly lateral. Finally, the bottom right figure shows a combination of respiratory motion between end-inhalation and end-exhalation and bulk motion.

Reconstructed PET images are shown in figure 7. Figures 7(a) and (b) show coronal and axial slices using different reconstruction methods. Motion-induced blurring artifacts are clearly visible on the NMC reconstruction primarily in the lateral direction, corresponding to bulk motion but also in the vertical direction due to respiratory motion. The gated reconstruction, which uses one sixth of the PET counts at a single body position, shows sharper features but is severely corrupted by noise. The motion-corrected reconstruction using XD-GRASP for motion estimation (denoted by MC-XDG) still shows noticeable motion artifacts because the XD-GRASP reconstruction failed to capture the bulk motion. The proposed method compensates both respiratory and bulk motion, significantly reducing motion-blur, while exhibiting a low noise level. Figure 7(c) shows line profiles through the kidney. Without motion correction, the activity peak is lowered by motion. Instead, two distinct peaks are visible, which correspond to the two bulk motion phases. The two peaks are also visible for the XD-GRASP based motion correction. The gated reconstructions and the motion-corrected reconstructions by the proposed method both preserve the peak activity. However, the gated reconstructions exhibit a high level of noise due to the reduced amount of data used for reconstruction.

Evaluation measures are reported in table 1. The table shows that motion corrected reconstruction leads to the highest CNR: a 83% improvement was observed over reconstruction without motion correction, 47% over XD-GRASP-based motion correction and 198% over gated reconstruction. The noise level in NMC and MC is similar (within 15%) but the contrast is substantially improved by motion correction, while the noise level in the gated reconstruction is three times higher leading to the low CNR. This is expected since gated reconstructions were not tuned to reduce noise but to increase contrast. One could expect a lower CNR for gated reconstruction with a tuned number of subsets and iterations. For the TBR, the gated reconstruction achieves the highest ratio, because gated reconstructions favor high contrast (at the expense of high noise). The proposed motion compensation method approaches the gated TBR (25% decrease) and outperforms NMC (20% increase).

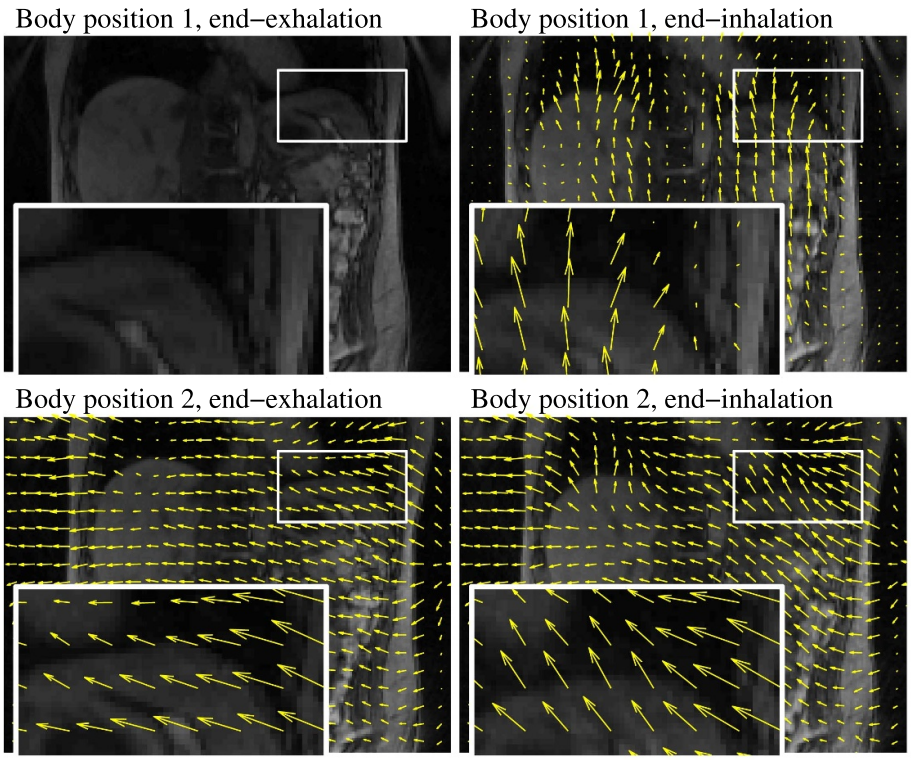

Figure 6. Estimated motion field between bins from different bulk motion phases. The top left panel corresponds to the bin used as reference (Body position 1 and the end of exhalation). The top right panel shows the same body position at the end of inhalation; the overlaid motion field exhibits mostly vertical displacement near the liver, corresponding to respiratory motion. The bottom row shows the estimated motion field at the end of exhalation and inhalation for the second body position (after bulk motion). Motion fields demonstrate the lateral displacement between body positions.

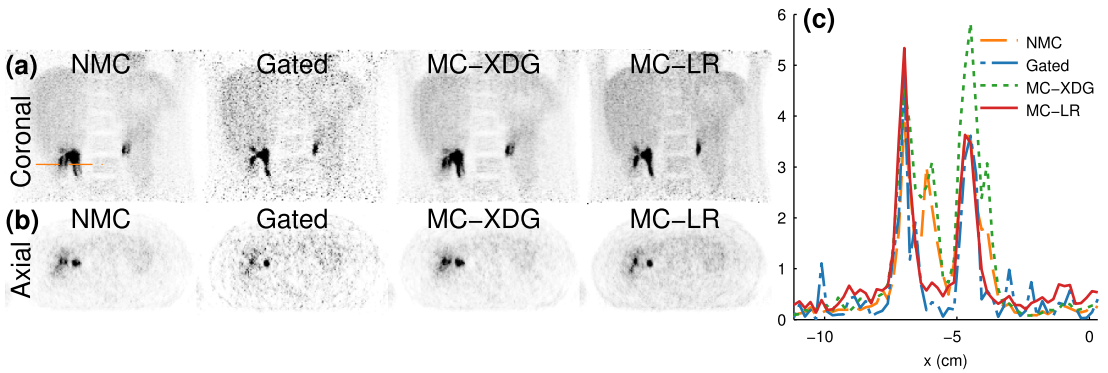

Figure 7. PET reconstructions for the bulk motion experiment using three different methods: reconstruction without motion correction (NMC), reconstruction from PET data corresponding to a single respiratory phase and body position (Gated), motion correction using motion estimated from the XD-GRASP MR reconstructions (MC-XDG) and proposed motion-corrected reconstruction from low-rank MR reconstruction (MC-LR). Profile plots through the right kidney (along the orange line drawn on the NMC image) are shown in (c).

3.2. Correction of irregular respiratory motion

The second experiment was designed to evaluate the performance of the proposed method in the case of irregular respiratory motion. The subject was instructed to alternate between slow deep and fast shallow breaths throughout the 5 minutes PET/MR acquisition.

MR images obtained by the proposed method are shown in figure 8. The top row shows images at different frames: two at the end of inhalation and two at the end of exhalation taken from different breathing patterns (deep/shallow), respectively. The full extent of the respiratory motion is captured and the images are artifacts-free. Figures 8(e) and (f) show 1D profiles of the image through the liver changing over time. Both the images and the plot in figure 8 clearly show the breathing patterns, alternating between deep slow breaths and fast shallow ones. Based on the reconstructed real-time MR images, 12 bins were determined through

Table 1. Contrast-to-noise ratio (CNR) and target-to-background ratio (TBR) for kidney region of interest. See figure 2 for a view of the regions of interest.

	NMC	Gated	MC-XDG	MC-LR
CNR	42.07	25.88	52.49	77.26
TBR	6.05	9.57	6.84	7.25

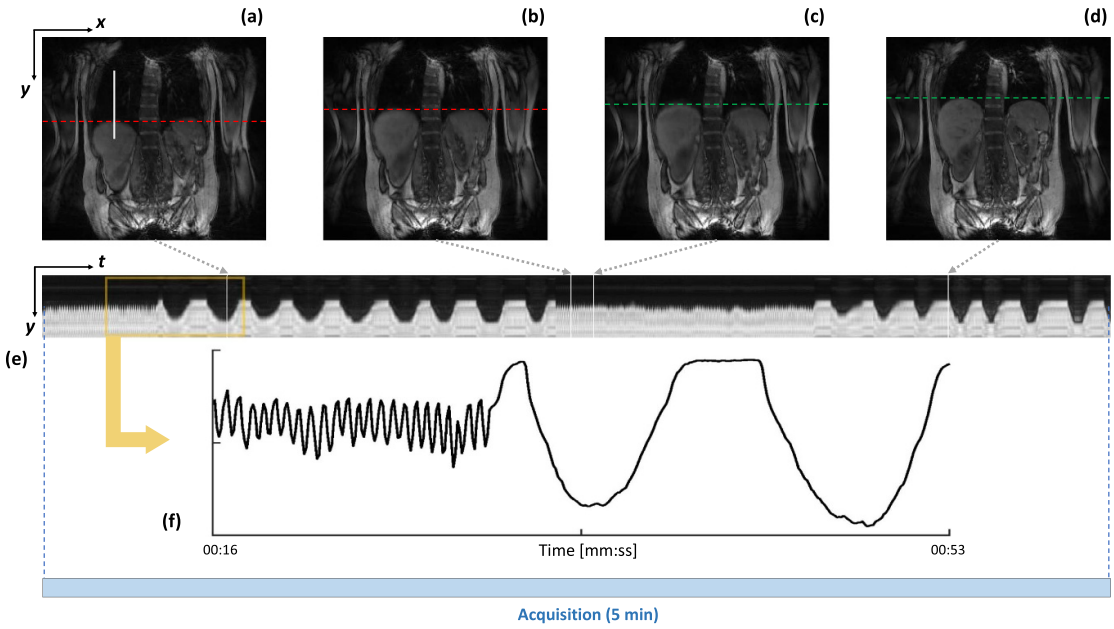

Figure 8. Reconstructed MR images in the case of irregular respiratory motion. The real-time profile (e) is plotted for a few minutes of the experiment where the subject changes their breathing pattern from slow and deep to fast and shallow respiration. Images (a) and (b) show representative images at end-inhalation during deep breath and shallow breath, respectively; (c) and (d) at end-exhalation. The red dashed-line indicates the top of the liver position for end-inhalation and the green dashed-line indicates the top of the liver position for end-exhalation for each breathing pattern.

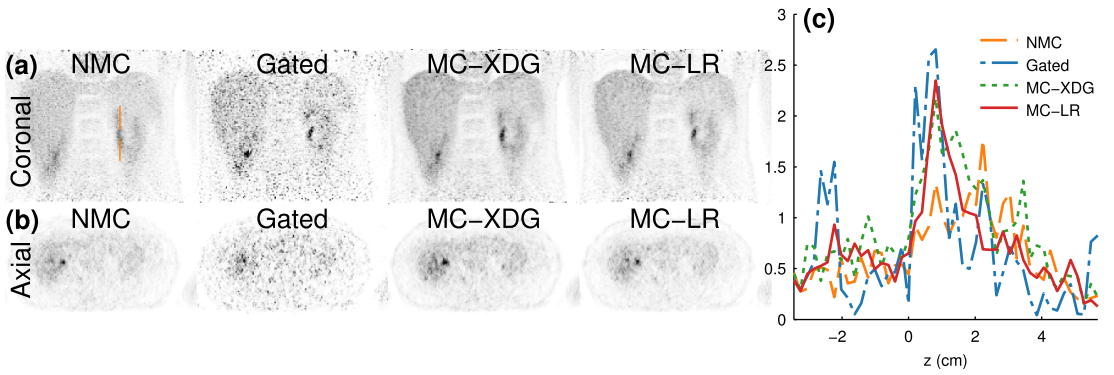

Figure 9. PET reconstructions for the irregular motion experiment using three different methods: reconstruction without motion correction (NMC), reconstruction from PET data corresponding to a single respiratory phase (Gated) and proposed motion-corrected reconstruction (MC-LR). (c) shows profile plots through the left kidney (the profile line is shown on the NMC coronal PET image).

analysis of the liver displacement in the MR images and were consequently used for motion field estimation and motion corrected PET reconstruction. Sequences of MR reconstructions are shown in Supplementary Material M2. Reconstructed MR images using XD-GRASP are shown in Supplementary Material M3, where the k-space data were grouped into 12 balanced bins to capture both deep and shallow respiratory motion.

Corresponding PET reconstructions are shown in figure 9. Images reconstructed without motion correction (NMC) exhibit blurring artifacts. This is particularly visible on the left kidney (see the orange line on the NMC coronal image) where the bright spot visible on other images is elongated in the vertical direction, due to the large amplitude of the respiratory motion. The gated reconstruction uses one sixth of the total number of counts and therefore is degraded by noise, despite resulting in a sharper image. The

Table 2. Contrast-to-noise ratio and target-to-background ratio for kidney region of interest. Regions are shown in figure 2.

	NMC	Gated	MC-XDG	MC-LR
CNR	17.52	15.28	37.39	46.18
TBR	3.92	9.00	6.33	7.64

motion corrected reconstructions using XD-GRASP and the proposed method for motion estimation both produce sharper images with higher SNR, while the proposed motion correction method results in the best image quality, in terms of noise and contrast. Corresponding line profiles are plotted in figure 9(c). The NMC peak is elongated along the y-axis, due to the large extent of the mostly vertical respiratory motion. The Gated line profile is sharper near its peak but has a large noise level. The proposed MC method results in a good compromise between sharpness and low noise. Contrast-to-noise and target-to-background ratios (defined in equations (9) and (10) respectively) are reported in table 2 (regions of interest are shown in figure 2(b)). Metrics show the superior performance of the proposed motion correction method. The improvement in CNR is around 163% over NMC and over 200% over gated reconstruction. As for the bulk motion experiment the gated reconstructions were tuned to maximize contrast rather than reduce noise. The CNR for the gated reconstructions could be improved with further tuning (*i.e.* by decreasing the number of subsets and iterations). The TBR for the proposed method is within 15% of the gated TBR and around 95% larger than NMC.

4. Discussions

We have demonstrated the performance of the proposed MR-based motion correction for PET in two challenging cases: bulk motion and irregular respiratory motion. The proposed subspace-based MR imaging method allows for reconstruction of high-resolution 3D volumes at a rate of 9.5 volume/s, which enables accurate motion field estimation even in the case of irregular motions. Another important benefit of the proposed approach is the ability to perform informed binning for PET motion correction, rather than relying on navigators or external markers which offer limited information on the subject motion. With full real-time volumetric MR images, detecting motion becomes straightforward, and the process of determining an appropriate number of bins is greatly simplified.

The key assumption of the subspace-based imaging method is the low-rank property of dynamic MR signals. We performed a simulation study to investigate this property in the case of regular and irregular respiratory motion. Two phantoms (shown in the Supplementary Material M4 and M5) were generated using the XCAT software (Segars *et al* 2010) to simulate regular and irregular respiratory motion. Respiratory and cardiac cycles were divided into respectively 30 and 40 phases and 3D volumes were computed for each respiratory and cardiac phase combination (*i.e.* 1200 volumes). A 4D (3D space + time) phantom was then built by selecting and concatenating frame by frame the 3D volumes based on simulated EKG and respiratory signals. Both the breathing frequency and diaphragm expansion were varied while keeping a constant heart rate in the simulation of the irregular respiratory motion. Each phantom contained six respiratory cycles. The contrast was designed to simulate a Balanced Steady-State Free Precession (bSSFP) signal for several compartments such as fat, muscles, etc. using T1 and T2 values from the literature (Bojorquez *et al* 2017). SVD was then performed to investigate the effect of an irregular respiratory pattern on the rank, and its corresponding approximation error with low-rank truncation (see Supplementary Material figure M6). The decay of the calculated singular values from both phantoms was very similar, indicating that the breathing pattern does not substantially affect the rank of the data.

The proposed method utilizes an MR acquisition which fully overlaps with the PET acquisition and provides real-time MR images for motion correction. The proposed method can still have benefits for other commonly used acquisition protocols. It is common in practice to reserve a first part of the PET acquisition to perform MR motion field measurements and use the remaining PET acquisition time to perform additional MR measurements (e.g. using T1 or T2 contrast sequences) that can be used for other diagnostic tasks (Petibon *et al* 2019). The proposed method can advantageously replace the motion field measurement sequence, possibly reducing the acquisition time while preserving image quality. A gating signal (e.g. navigator or external marker) can then be used in subsequent MR sequences to select an appropriate bin for each PET frame. Another approach is to integrate contrast sequences into the motion field estimation sequence described in this paper. This is under investigation and will be reported in separate publications.

The study reported in this paper has several limitations. First, the computation time for the low-rank reconstruction with sparsely sampled non-Cartesian k-space data could be a concern. The current MATLAB (The MathWorks, Inc. Natick, Massachusetts, United States) implementation performs reconstruction of one

slice and one coil in around one hour. We anticipate that using a lower level programming language and parallel computing devices (e.g. GPU) will help achieve reasonable runtimes (Wu *et al* 2011). Second, the proposed method does not have sufficient temporal resolution to resolve the motion in the transition phase between the two bulk motion phases of experiment 1 (figure 5(e)). The time-varying profile plot shows that the image quality in the transition is severely degraded. The corresponding list-mode data were excluded from the PET reconstruction. Since the duration of the bulk motion was short, only about 5% of the list-mode data were discarded and thus should not be a significant limitation. Third, this study focuses on demonstrating the feasibility of using subspaced-based real-time MR for PET motion correction. We showed the performance of our method in two cases (bulk motion and irregular respiratory motion) from *in vivo* PET/MR experiments on a healthy subject. More subjects are needed to fully evaluate the performance of the proposed method in clinical settings. It is also worthwhile to explore incorporating advanced system modeling including time-of-flight information and point-spread function modeling into the proposed method. While advanced imaging models are expected to improve low-count (e.g. gated) reconstructions and quantitative metrics, all reconstruction methods, including the proposed motion correction, would benefit from more accurate modeling.

5. Conclusion

We proposed an MR-based method for PET motion correction using a subspace-based real-time MR imaging for motion field estimation. We demonstrate the feasibility of the proposed method using ^{18}F-FDG-PET/MR studies on a healthy subject. Our results show that the proposed method can capture and correct for normal and irregular respiratory motions as well as bulk body motion. The proposed method can be beneficial to a range of clinical applications where irregular motion patterns are expected.

Acknowledgment

This work was supported in part by the National Institutes of Health under award numbers: T32EB013180, R01CA165221, R01HL118261, R21MH121812, R01HL137230 and P41EB022544.

ORCID iDs

Thibault Marin https://orcid.org/0000-0002-8669-1003
Yanis Djebra https://orcid.org/0000-0003-0756-571X
Paul K Han https://orcid.org/0000-0003-1650-1347
Isabelle Bloch https://orcid.org/0000-0002-6984-1532
Georges El Fakhri https://orcid.org/0000-0002-9005-6993
Yoann Petibon https://orcid.org/0000-0003-3067-4607

References

Bojorquez J Z, Bricq S, Acquitter C, Brunotte F, Walker P M and Lalande A 2017 What are normal relaxation times of tissues at 3T *Magn. Reson. Imaging* **35** 69–80

Boyd S, Parikh N, Chu E, Peleato B and Eckstein J 2011 Distributed optimization and statistical learning via the alternating direction method of multipliers *Found. Trends Mach. Learn.* **3** 1–122

Catana C 2015 Motion correction options in PET/MRI *Semin. Nucl. Med.* **45** 212–23

Christodoulou A G, Hitchens T K, Wu Y L, Ho C and Liang Z P 2014 Improved subspace estimation for low-rank model-based accelerated cardiac imaging *IEEE Trans. Biomed. Eng.* **61** 2451–7

Chun S Y and Fessler J A 2009 A simple regularizer for B-spline nonrigid imageregistration that encourages local invertibility *IEEE J. Sel. Top. Signal Process.* **3** 159–69

Dawood M, Buther F, Jiang X and Schafers K P 2008 Respiratory motion correction in 3-D PET data with advanced optical flow algorithms *IEEE Trans. Med. Imaging* **27** 1164–75

Feng L, Axel L, Chandarana H, Block K T, Sodickson D K and Otazo R 2016 XD-GRASP: Golden-angle radial MRI with reconstruction of extra motion-statedimensions using compressed sensing *Magn. Reson. Med.* **75** 775–88

Fessler J A and Sutton B P 2003 Nonuniform fast Fourier transforms using min-maxinterpolation *IEEE Trans. Signal Process.* **51** 560–74

Fulton R R, Meikle S R, Eberl S, Pfeiffer J, Constable C J and Fulham M J 2002 Correction for head movements in positron emission tomography using an optical motion-tracking system *IEEE Trans. Nucl. Sci.* **49** 116–23

Gillman A, Smith J, Thomas P, Rose S and Dowson N 2017 PET motion correction in context of integrated PET/MR: current techniques, limitations, and future projections *Med. Phys.* **44** e430–e445

Grimm R *et al* 2015 Self-gated MRI motion modeling for respiratory motion compensation in integrated PET/MRI *Medical Image Anal.* **19** 110–20

Huang C, Ackerman J L, Petibon Y, Normandin M D, Brady T J, El Fakhri G and Ouyang J 2014 Motion compensation for brain PET imaging using wireless MR active markers in simultaneous PET-MR: phantom and non-human primate studies *NeuroImage* **91** 129–37

Hudson H M and Larkin R S 1994 Accelerated image reconstruction using ordered subsets of projection data *IEEE Trans. Med. Imaging* **13** 601–9
Jin X, Mulnix T, Gallezot J D and Carson R E 2013 Evaluation of motion correction methods in human brain PET imaging-a simulation study based on human motion data *Med. Phys.* **40** 102503
Küstner T *et al* 2017 Respiratory gated PET derived in a fully automated manner from raw PET data *Medical Image Anal.* **42** 129–44
Kesner A L, Bundschuh R A, Detorie N C, Dahlbom M, Ziegler S I, Czernin J and Silverman D H 2009 MR-based respiratory and cardiac motion correction for PET imaging *IEEE Trans. Nucl. Sci.* **56** 677–86
Liang Z P 2007 Spatiotemporal imaging with partially separable functions *IEEE Int. Symp. on Biomedical Imaging' 2007 4th IEEE Int. Symp. on Biomedical Imaging: From Nano to Macro* pp 988–91
Liu C, Alessio A M and Kinahan P E 2011 Respiratory motion correction for quantitative PET/CT using all detected events with internal-external motion correlation *Med. Phys.* **38** 2715–23
Liu C, Pierce L A n, Alessio A M and Kinahan P E 2009 The impact of respiratory motion on tumor quantification and delineation in static PET/CT imaging *Phys. Med. Biol.* **54** 7345–62
Lu Y *et al* 2019 Data-driven voluntary body motion detection and non-rigid event-by-event correction for static and dynamic PET *Phys. Med. Biol.* **64** 065002
Montgomery A J, Thielemans K, Mehta M A, Turkheimer F, Mustafovic S and Grasby P M 2006 Correction of head movement on PET studies: comparison of methods *J. Nucl. Med.* **47** 1936–44
Munoz C, Neji R, Cruz G, Mallia A, Jeljeli S, Reader A J, Botnar R M and Prieto C 2018 Motion-corrected simultaneous cardiac positron emission tomography and coronary MR angiography with high acquisition efficiency, *Magn. Reson. Med.* **79** 339–50
Ouyang J, Li Q and El Fakhri G 2013 Magnetic resonance-based motion correction for positron emission tomography imaging *Semin. Nucl. Med.* **43** 60–7
Petibon Y, Guehl N J, Reese T G, Ebrahimi B, Normandin M D, Shoup T M, Alpert N M, El Fakhri G and Ouyang J 2016 Impact of motion and partial volume effects correction on PET myocardial perfusion imaging using simultaneous PET-MR *Phys. Med. Biol.* **62** 326–43
Petibon Y, Ouyang J, Zhu X, Huang C, Reese T G, Chun S Y, Li Q and El Fakhri G 2013 Cardiac motion compensation and resolution modeling in simultaneous PET-MR: a cardiac lesion detection study *Phys. Med. Biol.* **58** 2085–102
Petibon Y, Sun T, Han P K, Ma C, El Fakhri G and Ouyang J 2019 MR-based cardiac and respiratory motion correction of PET: application to static and dynamic cardiac (18)F-FDG imaging *Phys. Med. Biol.* **64** 195009
Rahmim A, Tang J and Zaidi H 2013 Four-dimensional image reconstruction strategies in cardiac-gated and respiratory-gated PET imaging *PET Clinics* **8** 51–67
Rank C M, Heußer T, Wetscherek A, Freitag M T, Sedlaczek O, Schlemmer H P and Kachelrieß M 2016 Respiratory motion compensation for simultaneous PET/MR based on highly undersampled MR data *Med. Phys.* **43** 6234
Robson P M, Trivieri M G, Karakatsanis N A, Padilla M, Abgral R, Dweck M R, Kovacic J C and Fayad Z A 2018 Correction of respiratory and cardiac motion in cardiac PET/MR using MR-based motion modeling *Phys. Med. Biol.* **63** 225011
Rubeaux M, Doris M K, Alessio A M and Slomka P J 2017 Enhancing cardiac PET by motion correction techniques *Current Cardiol. Rep.* **19** 14
Segars W P, Sturgeon G, Mendonca S B, Grimes J K and Tsui B M W 2010 4D XCAT phantom for multimodality imaging research *Med. Phys.* **37** 4902–15
Siddon R L 1985 Fast calculation of the exact radiological path for a three-dimensional CT array *Med. Phys.* **12** 252–5
Sun T, Petibon Y, Han P K, Ma C, Kim S J W, Alpert N M, El Fakhri G and Ouyang J 2019 Body motion detection and correction in cardiac PET: Phantom and human studies *Med. Phys.* **46** 4898–906
Werling A, Bublitz O, Doll J, Adam L E and Brix G 2002 Fast implementation of the single scatter simulation algorithm and its use in iterative image reconstruction of PET data *Phys. Med. Biol.* **47** 2947–60
Wu X L, Gai J, Lam F, Fu M, Haldar J P, Zhuo Y, Liang Z P, Hwu W M and Sutton B P 2011 Impatient MRI: Illinois Massively Parallel Acceleration Toolkit for image reconstruction with enhanced throughput in MRI 2011 *IEEE Int. Symp. on Biomedical Imaging: From Nano to Macro* pp 69–72
Yu Y *et al* 2016 Event-by-event continuous respiratory motion correction for dynamic PET imaging *J. Nucl. Med.* **57** 1084–90
Zhao B, Haldar J P, Christodoulou A G and Liang Z P 2012 Image reconstruction from highly undersampled (k,t)-space data with joint partial separability and sparsity constraints *IEEE Trans. Med. Imaging* **31** 1809–20